

Ab initio study of carrier mobility in $\text{Bi}_2\text{O}_2\text{Se}$

Yubo Yuan,^{1,2,3} Ziye Zhu,^{2,3} Jiaming Hu,^{2,3} and Wenbin Li^{2,3,*}

¹*School of Materials Science and Engineering, Zhejiang University, 310027 Hangzhou, China.*

²*Department of Materials Science and Engineering, Westlake University, 310030 Hangzhou, China.*

³*Key Laboratory of 3D Micro/Nano Fabrication and Characterization of Zhejiang Province,*

School of Engineering, Westlake University, 310030 Hangzhou, China.

(Dated: January 15, 2026)

$\text{Bi}_2\text{O}_2\text{Se}$ is an emerging high-performance layered semiconductor with excellent stability. While experimental studies have explored carrier transport across various doping levels for both *n*-type and *p*-type conduction, a comprehensive theoretical understanding remains incomplete. In this work, we present parameter-free first-principles calculations of the electron and hole mobilities in $\text{Bi}_2\text{O}_2\text{Se}$, based on iterative solution of the Boltzmann transport equation that includes electron-phonon scattering and ionized impurity scattering on an equal footing. Intriguingly, we find that $\text{Bi}_2\text{O}_2\text{Se}$ exhibits high electron mobilities in both the in-plane and out-of-plane directions, whereas the hole mobilities are only significant in the in-plane direction, displaying a unique three-dimensional (3D) electron transport and two-dimensional (2D) hole transport behavior. At 300 K, the calculated intrinsic electron and hole mobilities along the in-plane direction are $447 \text{ cm}^2 \text{ V}^{-1} \text{ s}^{-1}$ and $29 \text{ cm}^2 \text{ V}^{-1} \text{ s}^{-1}$, respectively, which are primarily affected by Fröhlich electron-phonon interactions. Due to its large static dielectric permittivity, $\text{Bi}_2\text{O}_2\text{Se}$ exhibits an exceptionally high low-temperature electron mobilities above $1.0 \times 10^5 \text{ cm}^2 \text{ V}^{-1} \text{ s}^{-1}$, and its electron mobilities above 50 K is robust against ionized impurity scattering over a wide range of impurity concentrations. By incorporating the Hall effect into our analysis, we predict an in-plane electron Hall mobility of $517 \text{ cm}^2 \text{ V}^{-1} \text{ s}^{-1}$ at 300 K, in excellent agreement with experimental data. These results provide valuable insights into the carrier transport mechanisms in $\text{Bi}_2\text{O}_2\text{Se}$, and offer predictive benchmarks for future theoretical and experimental investigations.

I. INTRODUCTION

Layered semiconductors have attracted significant research attention recently due to their promising applications in electronics and optoelectronics devices [1, 2]. Among them, $\text{Bi}_2\text{O}_2\text{Se}$ stands out as a layered semiconductor with excellent air stability and notable electronic and optical properties [3–5]. The bulk form of $\text{Bi}_2\text{O}_2\text{Se}$ is held together by weak interlayer electrostatic interactions and can be cleaved into thin two-dimensional (2D) layers [6]. Experimentally, thin layers of *n*-type $\text{Bi}_2\text{O}_2\text{Se}$ typically exhibit high room-temperature electron mobility ($\mu > 200 \text{ cm}^2 \text{ V}^{-1} \text{ s}^{-1}$) when the layer thickness exceeds 6 nm, and the low-temperature electron mobility can reach $10^4 \text{ cm}^2 \text{ V}^{-1} \text{ s}^{-1}$ or even higher [6–11]. On the other hand, intrinsic point defects can drive $\text{Bi}_2\text{O}_2\text{Se}$ into a highly insulating state, with the Fermi level located below the charge neutrality point, indicating *p*-type behavior [12]. Notably, *p*-type $\text{Bi}_2\text{O}_2\text{Se}$ transistors have been successfully fabricated via substitutional doping with Zn^{2+} , achieving a field-effect hole mobility up to $34 \text{ cm}^2 \text{ V}^{-1} \text{ s}^{-1}$ at 300 K [13].

Despite these promising experimental results, a rigorous theoretical understanding of carrier transport in $\text{Bi}_2\text{O}_2\text{Se}$, particularly regarding accurate mobility predictions, remains incomplete. The electron-phonon interaction plays a key role in determining the carrier transport properties of semiconductors. Previous DFT-based

studies have employed approaches of various approximation levels—such as the Bardeen-Shockley deformation potential theory for bulk, thin-layer, and nanoribbon structures of $\text{Bi}_2\text{O}_2\text{Se}$, and the semiclassical Boltzmann transport theory within the constant relaxation-time approximation—to investigate the phonon-limited electronic transport properties of $\text{Bi}_2\text{O}_2\text{Se}$ [14–18]. It should be noted that the deformation potential theory assumes acoustic phonons as the main source of carrier scattering, which is in general not valid in compound semiconductors with non-zero Born effective charges, as the contributions of optical phonons to carrier scattering are neglected [19]. In particular, polar optical phonons in compound semiconductors can generate long-range electrical potentials that couple strongly to electron motion [20]. Moreover, the carrier relaxation time in semiconductors is in general a function of both carrier energy and momentum, and a constant relaxation-time approximation is insufficient for accurate mobility predictions. Besides electron-phonon interaction, electron-ionized impurity interaction also plays a critical role in determining the carrier transport properties of doped semiconductors [21, 22]. A prior study by some of the authors [23] used the fully *ab initio* Boltzmann transport equation (BTE) within the self-energy relaxation time approximation (SERTA) to calculate the phonon-limited electron mobilities of $\text{Bi}_2\text{O}_2\text{Se}$, where the carrier lifetimes due to electron-phonon coupling were calculated fully from first principles, while a semi-empirical Brooks-Herring model was used to calculate momentum-dependent ionized-impurity scattering. The latter was combined with the BTE to calculate the the ionized-

* liwenbin@westlake.edu.cn

impurity-limited electron mobility. Total electron mobilities, accounting for both electron-phonon scattering and electron-ionized impurity scattering, were then estimated via Matthiessen's rule. This study revealed that Fröhlich interaction has a strong impact on electron transport in $\text{Bi}_2\text{O}_2\text{Se}$. Furthermore, the study revealed that the exceptionally high in-plane static dielectric constant ($\epsilon_0 > 150$) of $\text{Bi}_2\text{O}_2\text{Se}$ [23–26] leads to effective screening of Coulomb scattering potentials from ionized impurities in the material, contributing to its ultrahigh low-temperature electron mobility and defect-tolerant electron mobility at room temperature. Recent experimental progress in fabricating *p*-type $\text{Bi}_2\text{O}_2\text{Se}$ [13] further motivated the study of hole transport in $\text{Bi}_2\text{O}_2\text{Se}$. However, a first-principles investigation of hole mobility and transport mechanism in $\text{Bi}_2\text{O}_2\text{Se}$ is still lacking.

Moreover, recent years have seen notable progress in predicting the carrier mobility of semiconductors with greater accuracy and comprehensiveness. For example, the inclusion of dynamical quadrupole corrections were found to be important for accurate modeling of electron-phonon interactions in the carrier transport of certain semiconductors [27–30]. With respect to the numerical solution of the BTE, although the use of Cauchy-distributed sampling at the Brillouin zone center for both \mathbf{k} -points and \mathbf{q} -points in SERTA enables more efficient calculations, SERTA can exhibit considerable errors when compared with more accurate iterative solution of the BTE for polar semiconductors [31]. In addition, a first-principles treatment of ionized impurity scattering that accounts for the band structures, Kohn-Sham orbital overlaps, and anisotropic dielectric constants have recently been developed and implemented in the EPW code [22], opening opportunities for more accurate modeling of ionized-impurity scattering in semiconductors.

Leveraging these methodological advances, in this work we present a detailed first-principles investigation of electron and hole mobilities in bulk $\text{Bi}_2\text{O}_2\text{Se}$, utilizing a state-of-the-art iterative solution of the BTE that incorporates quadrupole corrections. Experimentally, mobility measurements for $\text{Bi}_2\text{O}_2\text{Se}$ were usually carried out on bulk or multilayer samples with a thickness above 6 nm, corresponding to ~ 10 layers [6–8]. For such a layer number, the intrinsic mobility of layered materials typically have already reached the corresponding bulk limit [32]. Therefore, our study of the transport properties of bulk $\text{Bi}_2\text{O}_2\text{Se}$ are still highly pertinent to the understanding of the experimental results. We further compare the calculated electron mobility to those obtained from approximate solutions of the BTE (such as SERTA), for a temperature range between 10 K to 400 K. At low temperatures, the total electron mobilities of $\text{Bi}_2\text{O}_2\text{Se}$ including both electron-phonon scattering and ionized-impurity scattering were predicted for electron concentrations from 10^{14} cm^{-3} to 10^{17} cm^{-3} . We find that $\text{Bi}_2\text{O}_2\text{Se}$ exhibits intrinsic three-dimensional (3D) electron and 2D hole transport, with polar optical phonons dominating the scattering processes for both electron and

hole transport at room temperature. We further predict in-plane electron Hall mobility of $\text{Bi}_2\text{O}_2\text{Se}$, which agrees well with a previous experimental result.

II. METHODS

A. Computational details

For the calculations of the basic electron and phonon properties of $\text{Bi}_2\text{O}_2\text{Se}$, we employed the density functional theory (DFT) and density functional perturbation theory (DFPT), as implemented in the Quantum ESPRESSO package [33, 34]. The generalized gradient approximation (GGA) of Perdew, Burke, and Ernzerhof (PBE) was used for the exchange-correlation functional [35]. Optimized norm-conserving Vanderbilt pseudopotentials were obtained from the PseudoDojo library [36, 37]. A plane-wave cutoff energy of 80 Ry was used for all calculations. The Brillouin zone was sampled using an $8 \times 8 \times 8$ \mathbf{k} -point grid, and a $4 \times 4 \times 4$ phonon \mathbf{q} -point grid was employed for DFPT calculations.

Calculations of electron-phonon coupling and carrier mobility were performed using the EPW package [38–41], and the maximally localized Wannier function method was applied using the Wannier90 software [42]. Carrier mobilities for both electrons and holes were computed by solving the iterative BTE [43, 44]. The BTE method is computationally expensive, as it requires a uniform fine grid size across the Brillouin zone. The dynamical quadrupole tensor of $\text{Bi}_2\text{O}_2\text{Se}$ was evaluated using DFPT as implemented in the ABINIT code [45–50]. To compute Hall mobility [29, 44], a magnetic field of 10^{-10} T was applied on $\text{Bi}_2\text{O}_2\text{Se}$. Adaptive broadening was employed to approximate Dirac delta functions [29]. The carrier concentration of $\text{Bi}_2\text{O}_2\text{Se}$ was set to 10^{14} cm^{-3} for calculations of intrinsic phonon-limited mobility. To capture the effect of ionized impurity scattering [22], the doping concentration was further increased to 10^{17} cm^{-3} . We employ the monopole approximation to describe the potential of an impurity of charge Ze , which was set to $Z = 1$ throughout the calculations.

For the convergence of intrinsic electron mobility, in the temperature range of 200–400 K, an energy window of 0.3 eV was applied and a fine Brillouin zone grid of up to 200^3 was used. To achieve the convergence of electron mobilities at lower temperatures (below 200 K), a smaller energy window of 0.1 eV suffices (Fig. S1 [51]). In this case, the densest fine grid reaches 420^3 to converge electron mobility at 10 K, and the result was linearly extrapolated to the limit of an infinitely dense Brillouin zone grid. The small slopes of the linear fitting lines indicate good convergence (Fig. S2). Electron mobilities as the electron concentration ranged from 10^{14} cm^{-3} to 10^{17} cm^{-3} were also linearly extrapolated with respect to the size of the grid (Fig. S3). The convergence of the fine grid size for the hole mobility calculations in $\text{Bi}_2\text{O}_2\text{Se}$ was

achieved with a grid size of up to 90^3 , using an energy window of 0.3 eV (Fig. S4).

B. Theory of carrier mobility calculations

The low-field electron mobility is given by the following expression (a similar form applies for hole mobility) [19]:

$$\mu_{\alpha\beta} = \frac{-1}{\Omega_{uc} n_c} \sum_n \int \frac{d^3k}{\Omega_{BZ}} v_{n\mathbf{k}\alpha} \partial_{E_\beta} f_{n\mathbf{k}}, \quad (1)$$

where the Greek indices α and β run over the three Cartesian directions. The symbol n_c refers to the carrier concentration. The quantity $v_{n\mathbf{k}\alpha}$ represents the band velocity along the α direction for the Kohn-Sham state with band index n and wavevector \mathbf{k} . The volumes of the unit cell and the first Brillouin zone are represented by Ω_{uc} and Ω_{BZ} , respectively. $\partial_{E_\beta} f_{n\mathbf{k}}$ corresponds to the linear response of the electronic occupation of the state $n\mathbf{k}$ to the applied electric field E . Within the framework of the linearized BTE, $\partial_{E_\beta} f_{n\mathbf{k}}$ is derived as follows [19]:

$$\begin{aligned} \partial_{E_\beta} f_{n\mathbf{k}} = & e v_{n\mathbf{k}\beta} \frac{\partial f_{n\mathbf{k}}^0}{\partial \epsilon_{n\mathbf{k}}} \tau_{n\mathbf{k}} \\ & + \frac{2\pi \tau_{n\mathbf{k}}}{\hbar} \sum_{m\nu} \int \frac{d^3q}{\Omega_{BZ}} |g_{mn\nu}(\mathbf{k}, \mathbf{q})|^2 \\ & \times [(n_{\mathbf{q}\nu} + 1 - f_{n\mathbf{k}}^0) \delta(\epsilon_{n\mathbf{k}} - \epsilon_{m\mathbf{k}+\mathbf{q}} + \hbar\omega_{\mathbf{q}\nu}) \\ & + (n_{\mathbf{q}\nu} + f_{n\mathbf{k}}^0) \delta(\epsilon_{n\mathbf{k}} - \epsilon_{m\mathbf{k}+\mathbf{q}} - \hbar\omega_{\mathbf{q}\nu})] \partial_{E_\beta} f_{m\mathbf{k}+\mathbf{q}}, \end{aligned} \quad (2)$$

where e is the elementary charge, $f_{n\mathbf{k}}^0$ represents the Fermi-Dirac occupation of the state $n\mathbf{k}$ in the absence of an external electric field. The electron-phonon matrix elements $g_{mn\nu}(\mathbf{k}, \mathbf{q})$ describe the amplitude for an electron to scatter from the initial state $n\mathbf{k}$ to the final state $m\mathbf{k} + \mathbf{q}$ through the emission or absorption of a phonon with frequency $\omega_{\mathbf{q}\nu}$, and $\epsilon_{n\mathbf{k}}$ and $\epsilon_{m\mathbf{k}+\mathbf{q}}$ denote the Kohn-Sham eigenenergies of the respective states. The Bose-Einstein distribution is given by $n_{\mathbf{q}\nu}$, and $\tau_{n\mathbf{k}}$ denotes the scattering lifetime.

To reduce the computational cost of solving the BTE, the SERTA simplifies the BTE by neglecting the second term in Eq.(2). This approximation assumes that scattering out of a state $n\mathbf{k}$ is dominant and neglects scattering back into it. The momentum relaxation time approximation (MRTA) partially accounts for these neglected back-scattering processes, providing a more accurate estimate of transport properties than SERTA, though still an approximation to the full iterative BTE solution. [19]. The inverse of the partial scattering lifetime, $\tau_{n\mathbf{k} \rightarrow m\mathbf{k}+\mathbf{q}}^{-1}$, corresponds to the partial scattering rate and is given by the sum of the electron-phonon (ph) rate and electron-impurity (imp) scattering rate:

$$\tau_{n\mathbf{k} \rightarrow m\mathbf{k}+\mathbf{q}}^{-1} = \tau_{n\mathbf{k} \rightarrow m\mathbf{k}+\mathbf{q}}^{-1,ph} + \tau_{n\mathbf{k} \rightarrow m\mathbf{k}+\mathbf{q}}^{-1,imp}. \quad (3)$$

where the partial electron-phonon scattering rate is defined as:

$$\begin{aligned} \tau_{n\mathbf{k} \rightarrow m\mathbf{k}+\mathbf{q}}^{-1,ph} = & \frac{2\pi}{\hbar} \sum_{\nu} |g_{mn\nu}(\mathbf{k}, \mathbf{q})|^2 [(n_{\mathbf{q}\nu} + 1 - f_{m\mathbf{k}+\mathbf{q}}^0) \\ & \times \delta(\epsilon_{n\mathbf{k}} - \epsilon_{m\mathbf{k}+\mathbf{q}} - \hbar\omega_{\mathbf{q}\nu}) \\ & + (n_{\mathbf{q}\nu} + f_{m\mathbf{k}+\mathbf{q}}^0) \delta(\epsilon_{n\mathbf{k}} - \epsilon_{m\mathbf{k}+\mathbf{q}} + \hbar\omega_{\mathbf{q}\nu})]. \end{aligned} \quad (4)$$

For electron-ionized impurity scattering, the Kohn-Luttinger ensemble averaging method can be employed to compute the partial scattering rate due to randomly distributed ionized impurities [22]:

$$\begin{aligned} \tau_{n\mathbf{k} \rightarrow m\mathbf{k}+\mathbf{q}}^{-1,imp} = & n_{imp} \frac{2\pi}{\hbar} \left[\frac{e^2}{4\pi\varepsilon_0} \frac{4\pi Z}{\Omega_{uc}} \right]^2 \\ & \times \sum_{\mathbf{G} \neq -\mathbf{q}} \frac{|\langle \psi_{m\mathbf{k}+\mathbf{q}} | e^{i(\mathbf{q}+\mathbf{G}) \cdot \mathbf{r}} | \psi_{n\mathbf{k}} \rangle_{uc}|^2}{|(\mathbf{q} + \mathbf{G}) \cdot \epsilon_0 \cdot (\mathbf{q} + \mathbf{G})|^2} \\ & \times \delta(\epsilon_{n\mathbf{k}} - \epsilon_{m\mathbf{k}+\mathbf{q}}), \end{aligned} \quad (5)$$

where n_{imp} and Z denote the concentration and charge of ionized impurities. The ϵ_0 is the vacuum permittivity. The tensor ϵ_0 is the low-frequency dielectric constant, accounting for both electronic and ionic polarizability. The calculated dielectric constants of $\text{Bi}_2\text{O}_2\text{Se}$ are 156 in-plane and 83 out-of-plane, as obtained using the Quantum ESPRESSO package. These values are slightly lower than those reported in our previous study [23], where the dielectric constants were computed directly from analytical equations. However, this small difference arises from methodological variations and does not affect the validity or accuracy of the current transport calculations.

The Hall mobility is calculated under the influence of a small external magnetic field \mathbf{B} , which exerts a Lorentz force on the electrons, thereby affecting their mobility. The Hall mobility is expressed as:

$$\mu_{\alpha\beta\gamma}^{\text{Hall}} = \frac{-1}{\Omega_{uc} n_c} \sum_n \int \frac{d^3k}{\Omega_{BZ}} v_{n\mathbf{k}\alpha} [\partial_{E_\beta} f_{n\mathbf{k}}(B_\gamma) - \partial_{E_\beta} f_{n\mathbf{k}}], \quad (6)$$

where γ denotes the Cartesian components of the magnetic field. To obtain the Hall mobility, the BTE is solved as:

$$\begin{aligned} \left[1 - \frac{e}{\hbar} \tau_{n\mathbf{k}} (\mathbf{v}_{n\mathbf{k}} \times \mathbf{B}) \cdot \nabla_{\mathbf{k}} \right] \partial_{E_\beta} f_{n\mathbf{k}}(B_\gamma) = & e v_{n\mathbf{k}\beta} \frac{\partial f_{n\mathbf{k}}^0}{\partial \epsilon_{n\mathbf{k}}} \tau_{n\mathbf{k}} \\ & + \frac{2\pi \tau_{n\mathbf{k}}}{\hbar} \sum_{m\nu} \int \frac{d^3q}{\Omega_{BZ}} |g_{mn\nu}(\mathbf{k}, \mathbf{q})|^2 \\ & \times [(n_{\mathbf{q}\nu} + 1 - f_{n\mathbf{k}}^0) \delta(\epsilon_{n\mathbf{k}} - \epsilon_{m\mathbf{k}+\mathbf{q}} + \hbar\omega_{\mathbf{q}\nu}) \\ & + (n_{\mathbf{q}\nu} + f_{n\mathbf{k}}^0) \delta(\epsilon_{n\mathbf{k}} - \epsilon_{m\mathbf{k}+\mathbf{q}} - \hbar\omega_{\mathbf{q}\nu})] \partial_{E_\beta} f_{m\mathbf{k}+\mathbf{q}}(B_\gamma). \end{aligned} \quad (7)$$

The Hall mobility is directly related to the drift mobility through the Hall factor, which is defined as:

$$r_{\alpha\beta\gamma}^{\text{Hall}} = \frac{\mu_{\alpha\beta\gamma}^{\text{Hall}}}{\mu_{\alpha\beta}}. \quad (8)$$

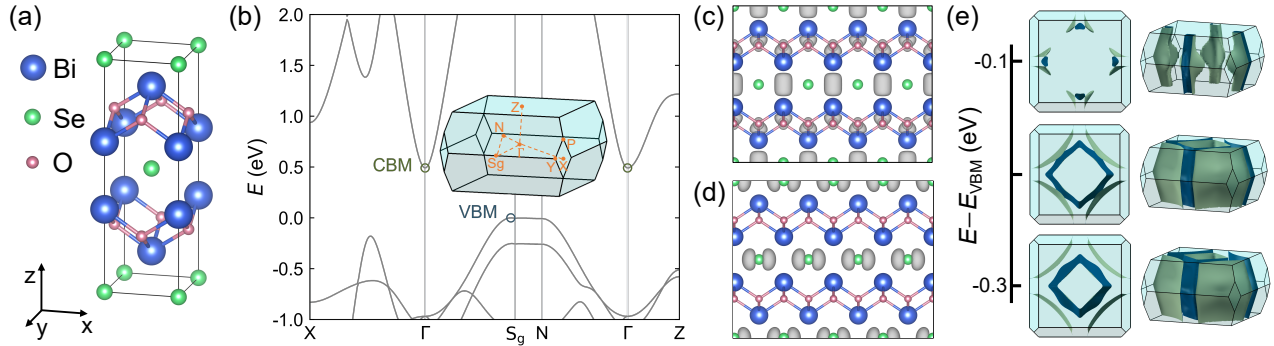


FIG. 1. (a) Atomistic structure of $\text{Bi}_2\text{O}_2\text{Se}$ in a tetragonal conventional unit cell. (b) Electronic band structure of $\text{Bi}_2\text{O}_2\text{Se}$, with the conduction band minimum (CBM) and valence band maximum (VBM) labeled. Inset shows the reciprocal space path employed in the band structure. (c) Isosurfaces of the electron wave function at the CBM (gray). (d) Isosurfaces of the hole wave function at the VBM (gray). (e) Evolution of the Fermi surfaces at energies of 0.1, 0.2, and 0.3 eV below the VBM, shown from bird's-eye views and side views of the Brillouin zones. The front- and back-side colors of Fermi surfaces are blue and green, respectively.

The Hall factor depends on both the material properties and temperature [52].

III. RESULTS AND DISCUSSION

$\text{Bi}_2\text{O}_2\text{Se}$ has a layered tetragonal structure in the conventional cell (Fig. 1(a)). In $\text{Bi}_2\text{O}_2\text{Se}$, the conduction band minimum (CBM) is located at the Γ point, as shown in Fig. 1(b). The second conduction band valley lies 400 meV above the CBM. At 400 K (the highest temperature considered in this study), the average thermal energy ($\frac{3}{2}k_{\text{B}}T$) corresponds to 52 meV, indicating that the available thermal energy is insufficient to promote electrons into the second valley. As a result, there are no accessible final states for electron intervalley scattering. Therefore, intravalley scattering dominates electron transport under low electric fields. The electronic bands near the CBM are primarily composed of Bi $6p$ orbitals, whereas those near the valence band maximum (VBM) mainly originate from O $2p$ and Se $4p$ orbitals (Fig. S5). Thus, Wannier functions including all of these p orbitals can fully capture the relevant bands (Fig. S6). Bi p orbital connectivity across layers reveals a three-dimensional character in the electron conducting states (Fig. 1(c)). The states at the VBM are primarily derived from Se p orbitals towards the in-plane direction (Fig. 1(d)). The ellipsoidal electron pocket near the CBM is localized at the center of the Brillouin zone (Fig. S7) [53]. However, as the eigenenergies near the VBM decrease, the hole pockets in the Brillouin zone initially appear near the four edges, and then interconnect and evolve into split, warped square shapes, as shown in Fig. 1(e). The shapes of the calculated Fermi surfaces near the VBM are consistent with those previously observed by angle-resolved photoemission spectroscopy [54].

We employ first-principles calculations to predict the intrinsic phonon-limited electron mobility. Fig. 2 presents

the electron mobilities from 10 K to 400 K. The calculated BTE electron mobilities along both the out-of-plane and in-plane directions remain high across the entire temperature range, indicating 3D electron transport. We further compare the exact BTE solution with approximation methods. The in-plane mobilities obtained using the MRTA and SERTA were tested for convergence with respect to the \mathbf{k} - and \mathbf{q} -point grid size, which were randomly distributed around the Γ point with a Cauchy distribution (Fig. S8). When the number of fine \mathbf{k} - and \mathbf{q} -point grid size reaches ~ 35000 , the in-plane mobilities calculated using MRTA show good agreement with the BTE results over the temperature range of 50–400 K. However, below 50 K, the electron mobilities predicted by MRTA tend to be lower than those obtained from the full BTE. In contrast, the SERTA consistently underestimates the in-plane electron mobilities across the entire temperature range.

N -type conductivity in $\text{Bi}_2\text{O}_2\text{Se}$ can be induced by intrinsic defects or ionized impurities [55, 56]. As the electron concentration increases, $\text{Bi}_2\text{O}_2\text{Se}$ gradually becomes a degenerate semiconductor, with the Fermi level shifting into the conduction band [57]. Fig. 3(a) shows that the temperature at which the $\text{Bi}_2\text{O}_2\text{Se}$ becomes a degenerate semiconductor decreases from 225 K to 50 K as the doping concentration is reduced from 10^{18} cm^{-3} to 10^{17} cm^{-3} . $\text{Bi}_2\text{O}_2\text{Se}$ remains semiconducting above 10 K at lower electron concentrations. In the metallic regime for electron concentrations equal to or greater than 10^{18} cm^{-3} , the plasmon energy exceeds the vibrational energy of the Fröhlich longitudinal optical (LO) phonon mode, more sophisticated modeling of free-carrier screening is necessary to predict phonon-limited electron mobility accurately [23, 58]. Consequently, we limit our investigation to the low-temperature electron mobilities over a doping range from 10^{14} cm^{-3} to 10^{17} cm^{-3} . In Figure 3(b), at a carrier concentration of 10^{17} cm^{-3} , the phonon-limited electron mobility exhibits a notice-

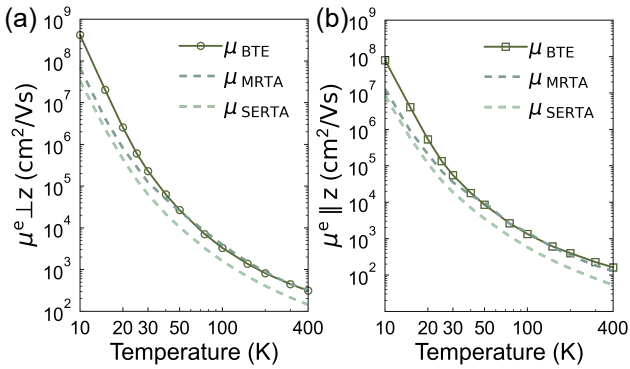


FIG. 2. (a) Temperature dependence of the in-plane intrinsic phonon-limited electron mobilities. In-plane mobilities are compared with momentum relaxation-time approximation (MRTA) and self-energy relaxation-time approximation (SERTA). (b) Temperature dependence of the out-of-plane intrinsic phonon-limited electron mobilities. Out-of-plane mobilities are compared with momentum relaxation-time approximation (MRTA) and self-energy relaxation-time approximation (SERTA).

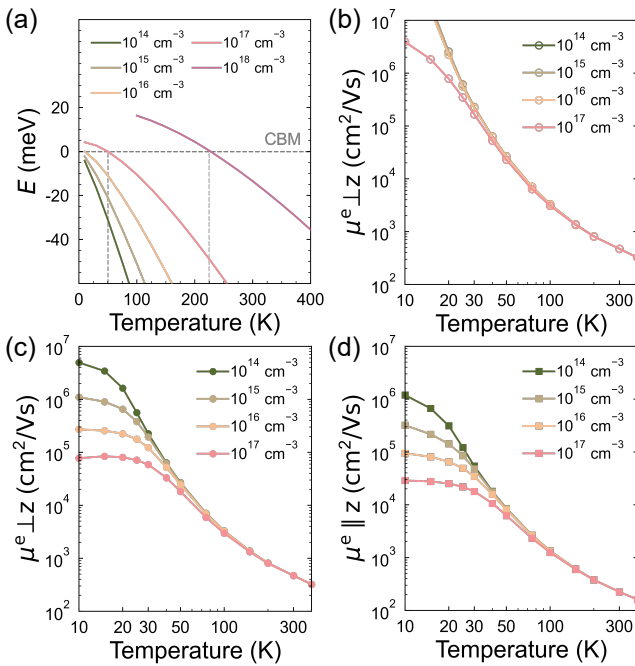


FIG. 3. (a) Temperature dependence of the Fermi level for ionized impurity concentrations ranging from 10^{14} cm⁻³ to 10^{18} cm⁻³, with the conduction band minimum set to zero. (b) Temperature dependence of in-plane intrinsic phonon-limited electron mobilities. (c) Temperature dependence of in-plane total electron mobilities, including both phonon and ionized impurity scattering. (d) Temperature dependence of out-of-plane total electron mobilities, including both phonon and ionized impurity scattering. In (b), (c), and (d), ionized impurity concentrations range from 10^{14} cm⁻³ to 10^{17} cm⁻³.

able decline, which can be attributed to the decrease of

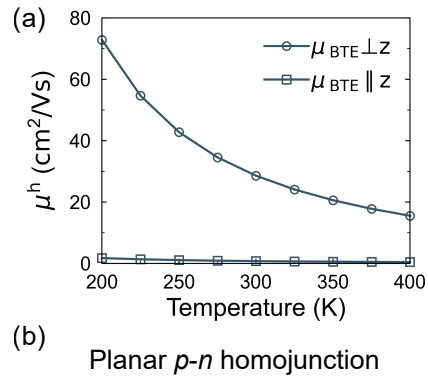


FIG. 4. (a) Temperature dependence of the in-plane and out-of-plane hole mobilities when the carrier concentration is 10^{14} cm⁻³. (b) Schematic diagram illustrating a planar *p*-*n* junction of $\text{Bi}_2\text{O}_2\text{Se}$.

electron average mean free path due to more efficient electron-phonon scattering rates.

Nevertheless, at low temperatures, ionized impurity scattering becomes a dominant factor influencing electron mobility, in addition to electron-phonon scattering [23]. To further investigate the total electron mobilities, we consider both phonon and ionized impurity scattering mechanisms, as shown in Fig. 3(c) and Fig. 3(d). The high total electron mobilities are indicative of weak ionized impurity scattering, due to the strong dielectric screening of the Coulomb potential from ionized impurities [23]. It is important that plateaus in total mobilities are observed at low temperatures (around 10–30 K) as the electron concentration increases, consistent with trends reported in experimental studies [7]. At 10 K and an electron concentration of 10^{17} cm⁻³, the in-plane and out-of-plane total mobilities reach 7.7×10^4 and 2.9×10^4 cm² V⁻¹ s⁻¹, respectively. The total electron mobilities of $\text{Bi}_2\text{O}_2\text{Se}$ remain nearly unchanged above 50 K regardless of the ionized impurity concentration, primarily due to the dominance of electron-phonon scattering over ionized impurity scattering. This behavior contrasts with that of silicon and other conventional semiconductors with typical low static dielectric constants, where ionized impurities can significantly reduce the total electron mobility [22]. At room temperature, our full BTE calculations yield electron mobilities of 447 cm² V⁻¹ s⁻¹ along the in-plane direction and 227 cm² V⁻¹ s⁻¹ along the out-of-plane direction.

Next, we turn to the hole mobility. As shown in Figure 4(a), the in-plane hole mobility at room temperature is predicted to be 29 cm² V⁻¹ s⁻¹, while the out-of-plane hole mobility is nearly zero. Although spin-orbit coupling (SOC) can significantly impact hole mo-

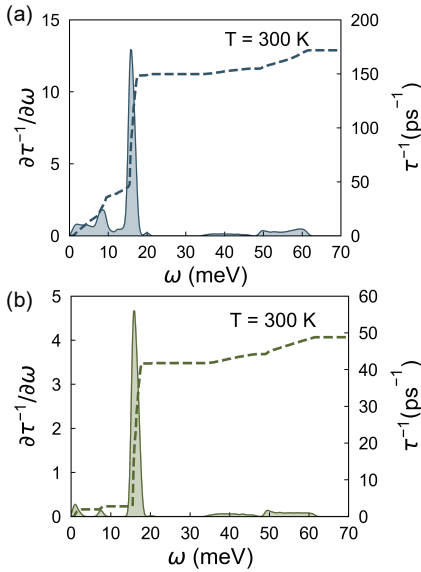


FIG. 5. (a) Spectral decomposition of the angularly averaged electron scattering rates as a function of phonon energy at 300 K, calculated using a fine 200^3 \mathbf{k} - and \mathbf{q} -point grid size. (b) Spectral decomposition of the angularly averaged hole scattering rates as a function of phonon energy at 300 K, calculated using a fine 90^3 \mathbf{k} - and \mathbf{q} -point grid size. In (a) and (b), dashed lines indicate the cumulative integrals of the scattering rates (axes on the right).

bilities in some semiconductors even with relatively small coupling strengths [29], it has a negligible effect on the band dispersion of $\text{Bi}_2\text{O}_2\text{Se}$ near the valence band edges and has a negligible effect on the hole transport properties of $\text{Bi}_2\text{O}_2\text{Se}$ (Fig. S9). Specifically, comparison with the BTE solutions including SOC shows that the in-plane electron mobilities computed without SOC exhibits an average error of only 5.6% over the range of 200–400 K. Considering the excellent in-plane electron and hole mobilities, we propose a planar p - n homojunction of $\text{Bi}_2\text{O}_2\text{Se}$, as illustrated in Fig. 4(b).

Fig. 5(a) presents the spectral decomposition of angularly averaged electron-phonon scattering rates as a function of phonon frequency at 300 K, evaluated for electrons located 39 meV ($\frac{3}{2}k_B T$) above the CBM. The total electron scattering rate is found to be 49 ps^{-1} . High-energy optical phonon branches (above 30 meV) contribute weakly to electron scattering across a broad frequency range. In contrast, three peaks are identified below 20 meV, corresponding to the longitudinal acoustic (LA), transverse optical (TO), and LO phonon modes, listed in order of increasing frequency. The LO phonon mode contributes approximately 80% of the total scattering, highlighting the dominant role of the Fröhlich interaction in electron-phonon scattering. By comparison, the LA and TO modes contribute only 4.0% and 1.7%, respectively. To assess the effect of the dynamical quadrupole correction, we recompute the electron scattering rates without including it. In this case, the to-

tal scattering rate becomes 48 ps^{-1} , consistent with our prior estimate of 50 ps^{-1} obtained using Cauchy sampling, also neglecting quadrupole corrections [23]. The contributions from the LA and TO modes are reduced to 1.7% and 0.8%, respectively, as shown in Fig. S10. Previous studies [27, 29, 59] have demonstrated that in certain polar materials, quadrupole corrections predominantly influence acoustic rather than optical phonons. In the case of $\text{Bi}_2\text{O}_2\text{Se}$, the small contribution of acoustic modes to the total scattering explains why electron mobilities remain largely unaffected by the quadrupole corrections. Nevertheless, the relative importance of these low-frequency acoustic and optical modes is expected to increase at low temperatures, where the population of LO phonons is significantly reduced. It should be noted that some previous studies reported the change from polar optical phonon (POP) scattering to piezoelectric scattering at low temperatures in few-layer flakes, which can be associated with the polar nature of the 2D ferroelectric material [60, 61]. This behavior is distinctly different from what we calculate for the bulk 3D phase in the paraelectric (PE) state. It possesses inversion symmetry in its PE state. As a result, the piezoelectric tensor is identically zero, and piezoelectric scattering is absent.

For the electron-phonon scattering mechanism of the hole carriers, we present the spectral decomposition of angularly averaged hole scattering rates by phonon frequencies at 300 K in Fig. 5(b), for holes at an energy of 39 meV below the VBM. The LO phonon mode shows strong coupling with holes, accounting for 60% of the total scattering rates. At lower frequencies, the spectral decomposition exhibits broad peaks, making it difficult to identify specific phonon modes. To analyze these modes in more detail, we plot the mode resolved electron-phonon matrix elements of $\text{Bi}_2\text{O}_2\text{Se}$ with the initial state at the VBM in Fig. S11. The LA phonon mode interacts with holes across a wide frequency range (0–12 meV), indicating that intravalley and intervalley scattering mediated by LA phonons contributes to the hole scattering. The total hole scattering rate is 172 ps^{-1} . The ultra-small out-of-plane hole mobility is primarily attributed to the large out-of-plane hole effective mass ($13.24m_0$). In contrast, the in-plane hole effective mass (m^*) is significantly smaller, with a value of $0.96m_0$ along the S_g – Γ path and $0.19m_0$ along the direction perpendicular to the S_g – Γ path. The harmonic average of the in-plane hole effective mass ($\overline{m^*}$) is $0.31m_0$. Using the simple Drude formula ($\mu = e/(m^* \cdot \tau^{-1})$), the calculated in-plane hole mobility is $33 \text{ cm}^2 \text{ V}^{-1} \text{ s}^{-1}$, which agrees well with our BTE results.

Finally, Hall mobility is generally measured over drift mobility for comparison with experimental data. Hence, Hall effect should be taken into account accordingly [29]. To ensure numerical accuracy, the Hall factor was linearly extrapolated with respect to the Brillouin zone grid size. The Hall factor is anisotropic, with the in-plane component being slightly higher than the out-of-plane component (Fig. S12). By combining the previously cal-

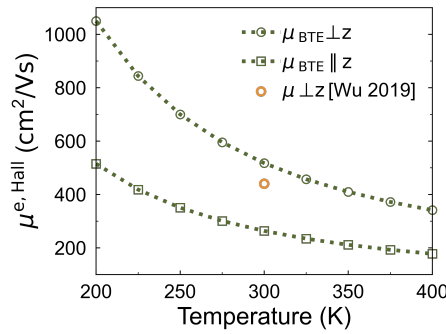


FIG. 6. Temperature dependence of electron Hall mobilities along the in-plane direction and along the out-of-plane direction from 200 K to 400 K. The experimental in-plane electron Hall mobility is at an electron concentration of $3 \times 10^{17} \text{ cm}^{-3}$ obtained from Ref. [62].

culated electron drift mobilities with the Hall factor, the Hall mobilities can be obtained, as shown in Fig. 6. At 300 K, the calculated in-plane electron Hall mobility is $517 \text{ cm}^2 \text{ V}^{-1} \text{ s}^{-1}$. This value is in good agreement with the experimental Hall mobility of $440 \text{ cm}^2 \text{ V}^{-1} \text{ s}^{-1}$ measured in a sample with a comparably low residual carrier concentration [62]. We do not compare with other experimental data, as most of the data are from a high-doping regime beyond the scope of our current model [63].

IV. CONCLUSIONS

In summary, we have carried out a comprehensive first-principles investigation of electron and hole transport in $\text{Bi}_2\text{O}_2\text{Se}$, employing an accurate iterative solution to the BTE with quadrupole corrections. Despite its layered structure, $\text{Bi}_2\text{O}_2\text{Se}$ exhibits excellent electron transport in both the in-plane and out-of-plane directions. Approximate methods such as SERTA and MRTA serve as efficient alternatives to the full BTE solution. However, they underestimate the in-plane electron mobilities, while MRTA results are consistent with the BTE calculations in the temperature range of 50–400 K. At low temperatures, we have predicted the total electron mobilities in n -type $\text{Bi}_2\text{O}_2\text{Se}$ limited by both electron-phonon scattering and ionized impurity scattering for carrier concentrations ranging from 10^{14} to 10^{17} cm^{-3} . At higher temperatures (200–400 K), electron-phonon scattering becomes the dominant mechanism. At 300 K, the intrinsic electron mobilities are predicted to be 447 and $227 \text{ cm}^2 \text{ V}^{-1} \text{ s}^{-1}$ for the in-plane and out-of-plane directions, respectively. The in-plane hole mobility is $29 \text{ cm}^2 \text{ V}^{-1} \text{ s}^{-1}$, while the out-of-plane hole mobility is nearly zero, owing to the large out-of-plane effective mass of holes. The efficient 3D electron and 2D hole transport suggest the feasibility of a planar p - n homojunction for future high-performance transistors. Moreover, the computed in-plane electron Hall mobility is $517 \text{ cm}^2 \text{ V}^{-1} \text{ s}^{-1}$,

aligned with experimental data. This work provides significant insights into the carrier transport and scattering mechanisms in the high-performance layered semiconductor $\text{Bi}_2\text{O}_2\text{Se}$, offering predictive benchmarks for the future development of $\text{Bi}_2\text{O}_2\text{Se}$ -based electronic and optoelectronic applications.

APPENDIX A: DYNAMICAL QUADRUPOLE TENSORS

The computed dynamical quadrupole tensors for $\text{Bi}_2\text{O}_2\text{Se}$ are listed in Table 1. The Se site, being inversion symmetric, has a vanishing quadrupole tensor. In contrast, the Bi and O sites lack inversion symmetry and thus exhibit generally nonzero components. Specifically, the Bi1 and O1 atoms transform into Bi2 and O2 aligned along the z direction under reflection across the xy -plane (see Fig. S14). Under this reflection, each occurrence of a z index in a tensor component introduces a sign change. For a given quadrupole tensor component $Q_{\alpha\beta\gamma}^{\kappa}$, where κ indexes atoms in the primitive cell of $\text{Bi}_2\text{O}_2\text{Se}$ and the rest of Greek indexes (α , β , and γ) indicate Cartesian directions, the relation between Bi1 (or O1) and Bi2 (or O2) is:

$$Q_{\alpha\beta\gamma}^{\text{Bi2/O2}} = (-1)^n Q_{\alpha\beta\gamma}^{\text{Bi1/O1}},$$

where n is the number of z indices among α, β, γ . Thus, quadrupole tensor components with an odd n change sign. The total sum of the quadrupole tensor components over all atoms in $\text{Bi}_2\text{O}_2\text{Se}$ vanishes, consistent with the absence of a third-rank piezoelectric tensor, which is subject to the same symmetry constraints. This is a consequence of the $I4/mmm$ space group and the presence of inversion symmetry in the crystal structure. Dynamical quadrupole corrections are included in all subsequent carrier mobility calculations unless stated otherwise.

TABLE I. Quadrupole tensor ($Q_{\alpha\beta\gamma}^{\kappa}$) of $\text{Bi}_2\text{O}_2\text{Se}$ (in e·Bohr).

κ	α	$\beta\gamma$					
		xx	yy	zz	yz, zy	xz, zx	xy, yx
Bi1	x	0.00	0.00	0.00	0.00	8.06	0.00
	y	0.00	0.00	0.00	8.06	0.00	0.00
	z	11.34	11.34	0.94	0.00	0.00	0.00
Bi2	x	0.00	0.00	0.00	0.00	-8.06	0.00
	y	0.00	0.00	0.00	-8.06	0.00	0.00
	z	-11.34	-11.34	-0.94	0.00	0.00	0.00
O1	x	0.00	0.00	0.00	0.00	13.59	0.00
	y	0.00	0.00	0.00	-13.59	0.00	0.00
	z	10.68	-10.68	0.00	0.00	0.00	0.00
O2	x	0.00	0.00	0.00	0.00	-13.59	0.00
	y	0.00	0.00	0.00	13.59	0.00	0.00
	z	-10.68	10.68	0.00	0.00	0.00	0.00
Se	x	0.00	0.00	0.00	0.00	0.00	0.00
	y	0.00	0.00	0.00	0.00	0.00	0.00
	z	0.00	0.00	0.00	0.00	0.00	0.00

ACKNOWLEDGMENTS

This work is supported by National Natural Science Foundation of China (Grant No. 62374136) and the Na-

tional Key R&D Program of China (2024YFA1409600). The authors thank the High-Performance Computing Center of Westlake University for technical assistance.

Data availability. The data that support the findings of this article are openly available [64].

[1] Y. Liu, X. Duan, H.-J. Shin, S. Park, Y. Huang, and X. Duan, Promises and prospects of two-dimensional transistors, *Nature* **591**, 43–53 (2021).

[2] K. S. Kim, J. Kwon, H. Ryu, C. Kim, H. Kim, E.-K. Lee, D. Lee, S. Seo, N. M. Han, J. M. Suh, J. Kim, M.-K. Song, S. Lee, M. Seol, and J. Kim, The future of two-dimensional semiconductors beyond moore’s law, *Nat. Nanotechnol.* **19**, 895–906 (2024).

[3] T. Li and H. Peng, 2D $\text{Bi}_2\text{O}_2\text{Se}$: An emerging material platform for the next-generation electronic industry, *Acc. Mater. Res.* **2**, 842–853 (2021).

[4] M. L. Li, P. Chen, Y. Zhao, M. Zhao, H. Q. Leng, Y. Wang, S. Ali, F. Raziq, X. Q. Wu, J. B. Yi, H. Y. Xiao, and L. Qiao, Materials properties and device applications of semiconducting bismuth oxyselenide, *InfoMat* **6**, e12539 (2024).

[5] C. Tan, J. Tang, X. Gao, C. Xue, and H. Peng, 2D bismuth oxyselenide semiconductor for future electronics, *Nat. Rev. Electr. Eng.* **2**, 494–513 (2025).

[6] C. Chen, M. X. Wang, J. X. Wu, H. X. Fu, H. F. Yang, Z. Tian, T. Tu, H. Peng, Y. Sun, X. Xu, J. Jiang, N. B. M. Schröter, Y. W. Li, D. Pei, S. Liu, S. A. Eka-hana, H. T. Yuan, J. M. Xue, G. Li, J. F. Jia, Z. K. Liu, B. H. Yan, H. L. Peng, and Y. L. Chen, Electronic structures and unusually robust bandgap in an ultrahigh-mobility layered oxide semiconductor, $\text{Bi}_2\text{O}_2\text{Se}$, *Sci. Adv.* **4**, eaat8355 (2018).

[7] J. X. Wu, H. T. Yuan, M. M. Meng, C. Chen, Y. Sun, Z. Y. Chen, W. H. Dang, C. W. Tan, Y. J. Liu, J. B. Yin, Y. B. Zhou, S. Y. Huang, H. Q. Xu, Y. Cui, H. Y. Hwang, Z. F. Liu, Y. L. Chen, B. H. Yan, and H. L. Peng, High electron mobility and quantum oscillations in non-encapsulated ultrathin semiconducting $\text{Bi}_2\text{O}_2\text{Se}$, *Nat. Nanotechnol.* **12**, 530 (2017).

[8] C. W. Tan, J. F. Jiang, J. Y. Wang, M. S. Yu, T. Tu, X. Y. Gao, J. C. Tang, C. C. Zhang, Y. C. Zhang, X. H. Zhou, L. M. Zheng, C. G. Qiu, and H. L. Peng, Strain-free layered semiconductors for 2D transistors with on-state current density exceeding $1.3 \text{ mA } \mu\text{m}^{-1}$, *Nano Lett.* **22**, 3770 (2022).

[9] C. Zhang, T. Tu, J. Wang, Y. Zhu, C. Tan, L. Chen, M. Wu, R. Zhu, Y. Liu, H. Fu, J. Yu, Y. Zhang, X. Cong, X. Zhou, J. Zhao, T. Li, Z. Liao, X. Wu, K. Lai, B. Yan, P. Gao, Q. Huang, H. Xu, H. Hu, H. Liu, J. Yin, and H. Peng, Single-crystalline van der Waals layered dielectric with high dielectric constant, *Nat. Mater.* **22**, 832–837 (2023).

[10] C. Tan, M. Yu, J. Tang, X. Gao, Y. Yin, Y. Zhang, J. Wang, X. Gao, C. Zhang, X. Zhou, L. Zheng, H. Liu, K. Jiang, F. Ding, and H. Peng, 2D fin field-effect transistors integrated with epitaxial high-k gate oxide, *Nature* **616**, 66–72 (2023).

[11] J. C. Tang, J. F. Jiang, X. Y. Gao, X. Gao, C. X. Zhang, M. D. Wang, C. Y. Xue, Z. R. Li, Y. L. Yin, C. W. Tan, F. Ding, C. G. Qiu, L. M. Peng, and H. L. Peng, Low-power 2D gate-all-around logics via epitaxial monolithic 3D integration, *Nat. Mater.* **24**, 519 (2025).

[12] T. Wang, Z. K. Xu, Z. Y. Zhu, M. Q. Wu, Z. F. Lou, J. L. Wang, W. H. Hu, X. H. Yang, T. Sun, X. R. Zheng, W. B. Li, and X. Lin, Highly insulating phase of $\text{Bi}_2\text{O}_2\text{Se}$ thin films with high electronic performance, *Nano Res.* **16**, 3224 (2023).

[13] Y.-J. Wang, J.-W. Zhang, J. Chen, H. Wang, S. Wu, C.-Y. Lo, J.-T. Hong, C.-Y. Syu, L.-S. Hao, I. S. Chen, Y.-C. Chang, Z. Yang, R. Huang, C.-L. Lin, P.-W. Chiu, Y.-L. Chueh, Y.-C. Chen, C.-H. Yeh, and Y.-H. Chu, Polarity modulation in compositionally tunable $\text{Bi}_2\text{O}_2\text{Se}$ thin films, *Nat. Commun.* **16**, 2873 (2025).

[14] J. Yu and Q. Sun, $\text{Bi}_2\text{O}_2\text{Se}$ nanosheet: An excellent high-temperature n-type thermoelectric material, *Appl. Phys. Lett.* **112**, 053901 (2018).

[15] C. Wang, G. Ding, X. Wu, S. Wei, and G. Gao, Electron and phonon transport properties of layered $\text{Bi}_2\text{O}_2\text{Se}$ and $\text{Bi}_2\text{O}_2\text{Te}$ from first-principles calculations, *New J. Phys.* **20**, 123014 (2018).

[16] N. Wang, M. Li, H. Xiao, H. Gong, Z. Liu, X. Zu, and L. Qiao, Optimizing the thermoelectric transport properties of $\text{Bi}_2\text{O}_2\text{Se}$ monolayer via biaxial strain, *Phys. Chem. Chem. Phys.* **21**, 15097–15105 (2019).

[17] X. Huang, C.-Y. Niu, J. Zhang, A. Wang, Y. Jia, and Y. Song, Strain-tunable electronic structure, optical response, and high electron mobility of $\text{Bi}_2\text{O}_2\text{Se}$ crystals, *APL Mater.* **7**, 081110 (2019).

[18] X. Huang, C.-Y. Niu, A. Wang, Y. Song, and Y. Jia, High-performance electron mobility and photoabsorption in $\text{Bi}_2\text{O}_2\text{Se}$ nanoribbons, *Appl. Phys. Lett.* **121**, 141902 (2022).

[19] S. Poncé, W. B. Li, S. Reichardt, and F. Giustino, First-principles calculations of charge carrier mobility and conductivity in bulk semiconductors and two-dimensional materials, *Rep. Prog. Phys.* **83**, 036501 (2020).

[20] C. Verdi and F. Giustino, Fröhlich electron-phonon vertex from first principles, *Phys. Rev. Lett.* **115**, 176401 (2015).

[21] I. T. Lu, J. J. Zhou, J. Park, and M. Bernardi, First-principles ionized-impurity scattering and charge transport in doped materials, *Phys. Rev. Mater.* **6**, L010801 (2022).

[22] J. Leveillee, X. Zhang, E. Kioupakis, and F. Giustino, Calculation of carrier mobility in semiconductors including ionized-impurity scattering, *Phys. Rev. B* **107**, 125207 (2023).

[23] Z. Y. Zhu, X. P. Yao, S. Zhao, X. Lin, and W. B. Li, Giant modulation of the electron mobility in semiconductor $\text{Bi}_2\text{O}_2\text{Se}$ via incipient ferroelectric phase transition, *J. Am. Chem. Soc.* **144**, 4541 (2022).

[24] Z. Xu, J. Wang, T. Wang, W. Hu, X. Yang, and X. Lin, Huge permittivity and premature metallicity in

Bi₂O₂Se single crystals, *Sci. China Phys. Mech. Astron.* **64**, 267312 (2021).

[25] Z. Zhu, J. Hu, Y. Yuan, H. Wang, X. Lin, and W. Li, Giant polarizability and origin of ferroelectricity in layered materials with a litharge-type structural unit, *Nano Lett.* **25**, 4093–4100 (2025).

[26] J. Zich, A. Sojka, P. Levinsk'y, M. M'išek, K.-H. Ahn, J. Navr'atil, J. Hejtm'anek, K. Kn'ižek, V. Hol'y, D. Nuzhnyy, F. Borodavka, S. Kamba, and v. Drašar, Phonon properties and unconventional heat transfer in a quasi-two-dimensional Bi₂O₂Se crystal, *Phys. Rev. Mater.* **9**, 054603 (2025).

[27] G. Brunin, H. P. C. Miranda, M. Giantomassi, M. Royo, M. Stengel, M. J. Verstraete, X. Gonze, G. M. Rignanese, and G. Hautier, Electron-phonon beyond Fröhlich: Dynamical quadrupoles in polar and covalent solids, *Phys. Rev. Lett.* **125**, 136601 (2020).

[28] V. A. Jhalani, J.-J. Zhou, J. Park, C. E. Dreyer, and M. Bernardi, Piezoelectric electron-phonon interaction from ab initio dynamical quadrupoles: Impact on charge transport in wurtzite gan, *Phys. Rev. Lett.* **125**, 136602 (2020).

[29] S. Poncé, F. Macheda, E. R. Margine, N. Marzari, N. Bonini, and F. Giustino, First-principles predictions of Hall and drift mobilities in semiconductors, *Phys. Rev. Res.* **3**, 043022 (2021).

[30] S. Poncé, M. Royo, M. Stengel, N. Marzari, and M. Gibertini, Long-range electrostatic contribution to electron-phonon couplings and mobilities of two-dimensional and bulk materials, *Phys. Rev. B* **107**, 155424 (2023).

[31] R. Claes, G. Brunin, M. Giantomassi, G. M. Rignanese, and G. Hautier, Assessing the quality of relaxation-time approximations with fully automated computations of phonon-limited mobilities, *Phys. Rev. B* **106**, 094302 (2022).

[32] W. Li, S. Poncé, and F. Giustino, Dimensional crossover in the carrier mobility of two-dimensional semiconductors: The case of inse, *Nano Lett.* **19**, 1774–1781 (2019).

[33] S. Baroni, S. de Gironcoli, A. Dal Corso, and P. Giannozzi, Phonons and related crystal properties from density-functional perturbation theory, *Rev. Mod. Phys.* **73**, 515 (2001).

[34] P. Giannozzi, O. Andreussi, T. Brumme, O. Bunau, M. B. Nardelli, M. Calandra, R. Car, C. Cavazzoni, D. Ceresoli, M. Cococcioni, N. Colonna, I. Carnimeo, A. Dal Corso, S. de Gironcoli, P. Delugas, R. A. DiStasio, A. Ferretti, A. Floris, G. Fratesi, G. Fugallo, R. Gebauer, U. Gerstmann, F. Giustino, T. Gorni, J. Jia, M. Kawamura, H. Y. Ko, A. Kokalj, E. Küçükbenli, M. Lazzeri, M. Marsili, N. Marzari, F. Mauri, N. L. Nguyen, H. V. Nguyen, A. Otero-de-la Roza, L. Paulatto, S. Poncé, D. Rocca, R. Sabatini, B. Santra, M. Schlipf, A. P. Seitsonen, A. Smogunov, I. Timrov, T. Thonhauser, P. Umari, N. Vast, X. Wu, and S. Baroni, Advanced capabilities for materials modelling with Quantum ESPRESSO, *J. Phys.: Condens. Matter* **29**, 465901 (2017).

[35] J. P. Perdew, K. Burke, and M. Ernzerhof, Generalized gradient approximation made simple, *Phys. Rev. Lett.* **77**, 3865 (1996).

[36] D. R. Hamann, Optimized norm-conserving Vanderbilt pseudopotentials, *Phys. Rev. B* **88**, 085117 (2013).

[37] M. J. van Setten, M. Giantomassi, E. Bousquet, M. J. Verstraete, D. R. Hamann, X. Gonze, and G. M. Rignanese, The PSEUDODOJO: Training and grading a 85 element optimized norm-conserving pseudopotential table, *Comput. Phys. Commun.* **226**, 39 (2018).

[38] F. Giustino, M. L. Cohen, and S. G. Louie, Electron-phonon interaction using Wannier functions, *Phys. Rev. B* **76**, 165108 (2007).

[39] H. Lee, S. Poncé, K. Bushick, S. Hajinazar, J. Lafuente-Bartolome, J. Leveillee, C. Lian, J. M. Lihm, F. Macheda, H. Mori, H. Paudyal, W. H. Sio, S. Tiwari, M. Zacharias, X. Zhang, N. Bonini, E. Kioupakis, E. R. Margine, and F. Giustino, Electron-phonon physics from first principles using the EPW code, *npj Comput. Mater.* **9**, 156 (2023).

[40] S. Poncé, E. R. Margine, C. Verdi, and F. Giustino, EPW: Electron-phonon coupling, transport and superconducting properties using maximally localized Wannier functions, *Comput. Phys. Commun.* **209**, 116 (2016).

[41] J. Noffsinger, F. Giustino, B. D. Malone, C. H. Park, S. G. Louie, and M. L. Cohen, EPW: A program for calculating the electron-phonon coupling using maximally localized Wannier functions, *Comput. Phys. Commun.* **181**, 2140 (2010).

[42] G. Pizzi, V. Vitale, R. Arita, S. Blügel, F. Freimuth, G. Géranton, M. Gibertini, D. Gresch, C. Johnson, T. Koretsune, J. Ibañez-Azpiroz, H. Lee, J.-M. Lihm, D. Marchand, A. Marrazzo, Y. Mokrousov, J. I. Mustafa, Y. Nohara, Y. Nomura, L. Paulatto, S. Poncé, T. Ponweiser, J. Qiao, F. Thöle, S. S. Tsirkin, M. Wierzbowska, N. Marzari, D. Vanderbilt, I. Souza, A. A. Mostofi, and J. R. Yates, Wannier90 as a community code: new features and applications, *J. Phys.: Condens. Matter* **32**, 165902 (2020).

[43] S. Poncé, E. R. Margine, and F. Giustino, Towards predictive many-body calculations of phonon-limited carrier mobilities in semiconductors, *Phys. Rev. B* **97**, 121201 (2018).

[44] F. Macheda and N. Bonini, Magnetotransport phenomena in *p*-doped diamond from first principles, *Phys. Rev. B* **98**, 201201 (2018).

[45] M. Royo and M. Stengel, First-principles theory of spatial dispersion: Dynamical quadrupoles and flexoelectricity, *Phys. Rev. X* **9**, 021050 (2019).

[46] X. Gonze, B. Amadon, G. Antonius, F. Arnardi, L. Baguet, J. M. Beuken, J. Bieder, F. Bottin, J. Bouchet, E. Bousquet, N. Brouwer, F. Bruneval, G. Brunin, T. Cavignac, J. B. Charraud, W. Chen, M. Côté, S. Cottenier, J. Denier, G. Geneste, P. Ghosez, M. Giantomassi, Y. Gillet, O. Gingras, D. R. Hamann, G. Hautier, X. He, N. Helbig, N. Holzwarth, Y. C. Jia, F. Jollet, W. Lafargue-Dit-Hauret, K. Lejaeghere, M. A. L. Marques, A. Martin, C. Martins, H. P. C. Miranda, F. Naccarato, K. Persson, G. Petretto, V. Planes, Y. Pouillon, S. Prokhorchenko, F. Ricci, G. M. Rignanese, A. H. Romero, M. M. Schmitt, M. Torrent, M. J. van Setten, B. Van Troeye, M. J. Verstraete, G. Zerah, and J. W. Zwanziger, The ABINIT project: Impact, environment and recent developments, *Comput. Phys. Commun.* **248**, 107042 (2020).

[47] X. Gonze, First-principles responses of solids to atomic displacements and homogeneous electric fields: Implementation of a conjugate-gradient algorithm., *Phys. Rev. B* **55**, 10337 (1997).

[48] X. Gonze and C. Lee, Dynamical matrices, Born effective charges, dielectric permittivity tensors, and interatomic

force constants from density-functional perturbation theory, *Phys. Rev. B* **55**, 10355 (1997).

[49] A. H. Romero, D. C. Allan, B. Amadon, G. Antonius, T. Applencourt, L. Baguet, J. Bieder, F. Bottin, J. Bouchet, E. Bousquet, F. Bruneval, G. Brunin, D. Caliste, M. Côté, J. Denier, C. Dreyer, P. Ghosez, M. Giantomassi, Y. Gillet, O. Gingras, D. R. Hamann, G. Hautier, F. Jollet, G. Jomard, A. Martin, H. P. C. Miranda, F. Naccarato, G. Petretto, N. A. Pike, V. Planes, S. Prokhorenko, T. Rangel, F. Ricci, G. M. Rignanese, M. Royo, M. Stengel, M. Torrent, M. J. van Setten, B. Van Troeye, M. J. Verstraete, J. Wiktor, J. W. Zwanziger, and X. Gonze, ABINIT: Overview and focus on selected capabilities, *J. Chem. Phys.* **152**, 124102 (2020).

[50] X. Gonze, F. Jollet, F. A. Araujo, D. Adams, B. Amadon, T. Applencourt, C. Audouze, J. M. Beuken, J. Bieder, A. Bokhanchuk, E. Bousquet, F. Bruneval, D. Caliste, M. Côté, F. Dahm, F. Da Pieve, M. Delaveau, M. Di Genaro, B. Dorado, C. Espejo, G. Geneste, L. Genovese, A. Gerossier, M. Giantomassi, Y. Gillet, D. R. Hamann, L. He, G. Jomard, J. L. Janssen, S. Le Roux, A. Levitt, A. Lherbier, F. Liu, I. Lukacevic, A. Martin, C. Martins, M. J. T. Oliveira, S. Poncé, Y. Pouillon, T. Rangel, G. M. Rignanese, A. H. Romero, B. Rousseau, O. Rubel, A. A. Shukri, M. Stankovski, M. Torrent, M. J. Van Setten, B. Van Troeye, M. J. Verstraete, D. Waroquiers, J. Wiktor, B. Xu, A. Zhou, and J. W. Zwanziger, Recent developments in the ABINIT software package, *Comput. Phys. Commun.* **205**, 106 (2016).

[51] See supplemental material at “****” for linear extrapolation of carrier mobility, k -/ q -grid and energy-window convergence tests, spin-orbit coupling, Wannier-interpolated band structures, mode-resolved electron-phonon coupling, orbitals projected on band structures, evolution of Fermi surface, linear extrapolation of Hall factor, phonon dispersion, and the labelled atoms in the rhombohedral primitive cell.

[52] R. Claes, S. Poncé, G. M. Rignanese, and G. Hautier, Phonon-limited electronic transport through first principles, *Nat. Rev. Phys.* **7**, 73 (2025).

[53] Y. Y. Lv, L. Xu, S. T. Dong, Y. C. Luo, Y. Y. Zhang, Y. B. Chen, S. H. Yao, J. Zhou, Y. S. Cui, S. T. Zhang, M. H. Lu, and Y. F. Chen, Electron-electron scattering dominated electrical and magnetotransport properties in the quasi-two-dimensional Fermi liquid single-crystal $\text{Bi}_2\text{O}_2\text{Se}$, *Phys. Rev. B* **99**, 195143 (2019).

[54] Y. Liang, Y. J. Chen, Y. W. Sun, S. P. Xu, J. X. Wu, C. W. Tan, X. F. Xu, H. T. Yuan, L. X. Yang, Y. L. Chen, P. Gao, J. D. Guo, and H. L. Peng, Molecular beam epitaxy and electronic structure of atomically thin oxyselenide films, *Adv. Mater.* **31**, 1901964 (2019).

[55] X. Ding, M. H. Li, P. Chen, Y. Zhao, M. Zhao, H. Q. Leng, Y. Wang, S. Ali, F. Raziq, X. Q. Wu, H. Y. Xiao, X. T. Zu, Q. Y. Wang, A. Vinu, J. B. Yi, and L. Qiao, $\text{Bi}_2\text{O}_2\text{Se}$: A rising star for semiconductor devices, *Matter* **5**, 4274 (2022).

[56] B. Zhan, S. Butt, Y. C. Liu, J. L. Lan, C. W. Nan, and Y. H. Lin, High-temperature thermoelectric behaviors of Sn-doped n -type $\text{Bi}_2\text{O}_2\text{Se}$ ceramics, *J. Electroceram.* **34**, 175 (2015).

[57] Z. K. Xu, J. L. Wang, T. Wang, W. H. Hu, X. H. Yang, and X. Lin, Huge permittivity and premature metallicity in $\text{Bi}_2\text{O}_2\text{Se}$ single crystals, *Sci. China Phys. Mech.* **64**, 267312 (2021).

[58] C. Verdi, F. Caruso, and F. Giustino, Origin of the crossover from polarons to Fermi liquids in transition metal oxides, *Nat. Commun.* **8**, 15769 (2017).

[59] A. M. D. Wang, K. Bushick, N. Pant, W. Lee, X. Zhang, J. Leveillee, F. Giustino, S. Poncé, and E. Kioupakis, Electron mobility of SnO from first principles, *Appl. Phys. Lett.* **124**, 172103 (2024).

[60] F. Yang, J. Wu, A. Suwardi, Y. Zhao, B. Liang, J. Jiang, J. Xu, D. Chi, K. Hippalgaonkar, J. Lu, and Z. Ni, Gate-tunable polar optical phonon to piezoelectric scattering in few-layer $\text{Bi}_2\text{O}_2\text{Se}$ for high-performance thermoelectrics, *Adv. Mater.* **33**, 2004786 (2021).

[61] W. H. Yip, Q. Fu, J. Wu, K. Hippalgaonkar, Z. Liu, X. Wang, M. Boutchich, and B. K. Tay, Few-layer $\text{Bi}_2\text{O}_2\text{Se}$: a promising candidate for high-performance near-room-temperature thermoelectric applications, *Nanotechnology* **35**, 465401 (2024).

[62] J. X. Wu, C. G. Qiu, H. X. Fu, S. L. Chen, C. C. Zhang, Z. P. Dou, C. W. Tan, T. Tu, T. R. Li, Y. C. Zhang, Z. Y. Zhang, L. M. Peng, P. Gao, B. H. Yan, and H. L. Peng, Low residual carrier concentration and high mobility in 2D semiconducting $\text{Bi}_2\text{O}_2\text{Se}$, *Nano Lett.* **19**, 197 (2019).

[63] M. Lin, L. Liao, D. Wu, Y. Huang, J. Wu, L. Wang, W. Xu, Y. Zhang, J. Song, Y. Zhang, and C. Li, 2D semiconductors directly grown on Si with room temperature mobility exceeding $2000 \text{ cm}^2 \text{ V}^{-1} \text{ s}^{-1}$, *Small* **21**, 2500026 (2025).

[64] Y. Yuan, <https://zenodo.org/records/15720251> (2025).